ENGINEERING Health and Rehabilitation Engineering
https://doi.org/10.2738/ENGHRE.2026.0013 ISSN 2097-7808
Original Research

Multi-joint Synergistic Isokinetic Training via a Variable-impedance Tunnel Constraint for Upper-limb Rehabilitation

Zhao LIU[1, 2], Jiexin ZHANG[3], Mingxiang LUO[1], Zixiang ZHOU[1], Tianrui WANG[1], Kaiyu HU[1], Yixuan SHENG[1], Zhen SONG[2], Honghai LIU (✉)[1, 2]

1 State Key Laboratory of Robotics and Systems (HIT), Harbin Institute of Technology (Shenzhen), Shenzhen 518055, China

2 Pengcheng Laboratory, Shenzhen 518055, China

3 State Key Laboratory of Intelligent Manufacturing Equipment and Technology, School of Mechanical Science and Engineering, Huazhong University of Science and Technology, Wuhan, Hubei 430074, China

ENG. Health Rehabil. Eng., **Just Accepted Manuscript** · https://doi.org/10.2738/ENGHRE.2026.0013

http://journal.hep.com.cn on November 10, 2026

© The Author(s) 2026. This article is published by Higher Education Press

Just Accepted

This is a “Just Accepted” manuscript, which has been examined by the peer-review process and has been accepted for publication. A “Just Accepted” manuscript is published online shortly after its acceptance, which is prior to technical editing and formatting and author proofing. Higher Education Press (HEP) provides “Just Accepted” as an optional and free service which allows authors to make their results available to the research community as soon as possible after acceptance. After a manuscript has been technically edited and formatted, it will be removed from the “Just Accepted” Web site and published as an Online First article. Please note that technical editing may introduce minor changes to the manuscript text and/or graphics which may affect the content, and all legal disclaimers that apply to the journal pertain. In no event shall HEP be held responsible for errors or consequences arising from the use of any information contained in these “Just Accepted” manuscripts. To cite this manuscript please use its Digital Object Identifier (DOI®), which is identical for all formats of publication.”

Multi-joint Synergistic Isokinetic Training via a Variable-impedance Tunnel Constraint for Upper-limb Rehabilitation

Zhao LIU[1, 2], Jiexin ZHANG[3], Mingxiang LUO[1], Zixiang ZHOU[1], Tianrui WANG[1], Kaiyu HU[1], Yixuan SHENG[1], Zhen SONG[2], Honghai LIU (✉)[1, 2]

1 State Key Laboratory of Robotics and Systems (HIT), Harbin Institute of Technology (Shenzhen), Shenzhen 518055, China

2 Pengcheng Laboratory, Shenzhen 518055, China

3 State Key Laboratory of Intelligent Manufacturing Equipment and Technology, School of Mechanical Science and Engineering, Huazhong University of Science and Technology, Wuhan, Hubei 430074, China

Correspondence: honghai.liu@icloud.com

Contact: Zhao LIU, phone: 13889470310, email: jason_creator@126.com

Abstract Conventional isokinetic dynamometers control angular velocity about a single joint axis, whereas functional upper-limb movements involve multiple joints. To address this limitation, this paper proposes multi-joint synergistic isokinetic training, an active-resistance approach implemented on a 3-DOF upper-limb exoskeleton with a variable-impedance tunnel constraint (VITC). A prescribed task-space velocity ceiling establishes isokinetic resistance, while the VITC permits voluntary spatial variation within a free-motion core and progressively activates corrective and safety constraints as deviation increases. The reconstructed end-effector speed approached the three nominal settings, with small peak overshoots at 0.10 and 0.15 m/s. In the perturbation trial, the maximum radial deviation was 104 mm, 4 mm beyond the nominal tunnel boundary. In a five-subject comparison with isotonic free-weight exercise, the proposed training produced higher muscle activation, with significant increases in the biceps and triceps brachii (t-test). These results demonstrate multi-joint synergistic isokinetic training as a new patient-active and multi-joint rehabilitation paradigm.

Keywords Upper-limb exoskeleton, Isokinetic training, Variable-impedance control, Task-oriented rehabilitation

1 Introduction

Stroke and other neurological injuries frequently leave survivors with persistent upper-limb motor impairment that limits independence in activities of daily living. Intensive, repetitive and task-oriented practice is a central principle of motor recovery, but delivering it manually is difficult to dose consistently. Robot-aided rehabilitation has therefore attracted sustained interest, because robotic devices can provide high-intensity, reproducible movement therapy while objectively quantifying patient performance [1,2]. The clinical evidence indicates that robot-assisted arm training can improve motor function after stroke [3], and the field has expanded from early end-effector (EE) manipulanda to a wide variety of devices for the upper limb [4,5].

Among the loading paradigms available for strength and motor training, isokinetic exercise occupies an important role. The isokinetic loading allows a muscle to be exercised near its maximal capacity throughout the range of motion while limiting the risk of injurious peak forces, which is particularly valuable for weak or recovering muscles [6–8]. Clinically, isokinetic dynamometry is also a standard tool for quantifying muscle strength and asymmetry [7]. Commercial dynamometers established this clinical standard but are bulky, costly, and built around a single rotational joint aligned with a fixed mechanical axis. These limitations have motivated the development of robotic isokinetic devices. Hu et al. [9] developed an elbow isokinetic muscle-strength trainer that infers the user's motion participation to plan the target speed and produce a dynamic damping effect. They use a linear extended-state observer to estimate and reject the training disturbance, thereby maintaining accurate speed control during active interaction. Feng et al. [10] developed a power-free knee robot for home-based isokinetic training and evaluated it in a six-week program involving patients after

knee surgery. Zhou et al. [11] built a lightweight upper-limb isokinetic device with joint-level torque estimation for early stroke rehabilitation. These systems illustrate joint-level approaches to robotic isokinetic training. However, they still drive one joint about a single axis and therefore cannot reproduce the coupled, multi-joint movements that characterize functional tasks such as reaching to the mouth.

Multi-joint synergistic isokinetic training is an active-resistance approach for functional movement, with "synergistic" referring to the coordinated participation of multiple joints. The prescribed limit applies to the magnitude of the end-effector's Cartesian linear velocity. Its purpose is to encourage maximal voluntary effort throughout the movement.

Multi-joint upper-limb exoskeletons can in principle deliver isokinetic loading along functionally relevant trajectories [12–14], but safe implementation requires a control strategy that mediates the physical interaction between the device and the patient. Impedance and admittance control provide a principled framework for regulating this interaction by shaping the dynamic relationship between motion and force rather than commanding either in isolation [15]. Realizing the ceiling velocity that defines isokinetic motion under an uncertain, patient-generated force is itself a control problem. Li et al. [16] reported a portable variable-impedance robot for isokinetic knee resistance training in young people with spinal muscular atrophy. Zarrin et al. [17] developed a variable-admittance controller for an upper-limb rehabilitation exoskeleton that tunes the admittance to each user. It promoted active participation while discouraging incorrect hand motion and arm posture. Building on the impedance and admittance framework, the assist-as-needed principle advocates supplying only as much support as the patient requires, so that residual volitional effort is preserved and over-reliance on the robot is avoided [18,19].

Recent patient-cooperative controllers often use trajectory constraints to guide and regulate patient motion. Onfiani et al. [20] proposed an admittance-type virtual fixture that constrains the EE to a prescribed geometric path and supports assistive and resistive modes while allowing the patient to regulate progression speed. Sun et al. [21] formulated virtually constrained admittance control that preserves permissible motion while rejecting motion transverse to the constraint manifold. Asl et al. [22] introduced field-based assist-as-needed control using a desired velocity field, whereas Liu et al. [23] constructed a virtual coordination tunnel with adaptive impedance to keep elbow-wrist motion within a coordination channel. However, their training tasks did not impose a movement-speed limit. Together with variable-admittance assist-as-needed approaches [17], these methods mainly regulate compliant or guided task execution and movement-pattern constraints rather than impose a speed ceiling for active isokinetic resistance.

Despite these advances, a distinct gap remains between patient-cooperative path guidance and isokinetic resistance training. Existing approaches may constrain motion direction, but their force-velocity behavior is not defined by an isokinetic ceiling. In contrast, isokinetic strengthening requires the user to voluntarily exert effort against a prescribed speed limit [6-8]. Extending this principle to multi-joint task space therefore requires two complementary constraints: 1) A maximum EE linear speed for isokinetic resistance; 2) An admissible spatial region for preserving the intended functional movement pattern and safety.

This paper implements multi-joint synergistic isokinetic training on an upper-limb exoskeleton. The controller uses an EE speed ceiling for active resistance and a variable-impedance tunnel constraint (VITC) to limit deviations from the intended movement pattern. The main contributions are as follows:

(1) We develop a 3-DOF upper-limb exoskeleton platform for multi-joint synergistic isokinetic training. The three actuated joints provide elbow flexion/extension (Joint 1), forearm pronation/supination (Joint 2), and wrist flexion/extension (Joint 3), and each joint carries a torque sensor that supports closed-form gravity compensation.

(2) We develop a VITC mechanism for movement-pattern regulation. The admissible corridor is divided into a free-motion isokinetic core, a variable-impedance shell, and an outer safety region, allowing small path deviations while progressively correcting excessive departures.

(3) We evaluate EE speed regulation and the tunnel response to lateral perturbations. A single-session study with five healthy male participants provides an exploratory within-participant comparison of acute sEMG amplitudes during exoskeleton exercise and isotonic free-weight exercise.

2 Methods

2.1 System description

As shown in Fig.1(a), the proposed multi-joint synergistic isokinetic training system consists of a 3-DOF upper-limb exoskeleton [24], a real-time embedded controller with a 50 Hz control loop, and a host PC for telemetry and visualization. The exoskeleton actuates elbow flexion/extension (Joint 1), forearm pronation/supination (Joint 2) and wrist flexion/extension (Joint 3). Each joint is equipped with a torque sensor, enabling joint-level state estimation and human–robot interaction torque measurement.



(a) (b)

Fig. 1. The 3-DOF upper-limb exoskeleton platform for multi-joint synergistic isokinetic training: (a) Prototype of the platform; (b) Kinematic model.

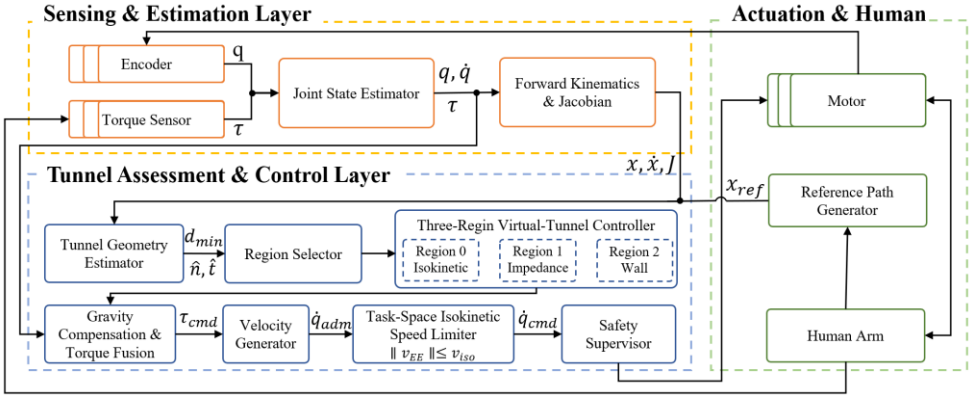


Fig. 2. Control architecture for multi-joint synergistic isokinetic training with the variable-impedance tunnel constraint.

The control architecture follows a hierarchical structure (Fig. 2). The sensing and estimation layer acquires joint positions and interaction torques and reconstructs the end-effector position, velocity, and Jacobian. Based on the reference path, the tunnel assessment and control layer evaluates the EE deviation and selects the corresponding isokinetic, impedance, or wall region. The gravity-compensated interaction torque is then converted into an admittance-based velocity command, whose commanded EE speed is limited by the prescribed ceiling. Finally, the safety supervisor constrains the commanded motion before execution by the actuators, while the tunnel controller regulates path deviation to limit departures from the intended movement pattern.

2.2 Kinematic modeling and joint-state estimation

As shown in Fig. 1(b), to establish the kinematic model of the exoskeleton, the Denavit–Hartenberg (DH) parameter method is used to define the relationships between joints, thereby yielding the mapping from joint space to Cartesian space. Here, d denotes the offset between joint 1 and joint 2, while L_1 and L_2 represent the

forearm length and palm length, respectively (both adjustable). Let $q = [q_1, q_2, q_3]^T$ denote the joint configuration. The EE position $p \in \mathbb{R}^3$ is obtained through a serial-chain forward kinematics (FK) model parameterized by the link geometry:

$$p = \mathrm{FK}(q) \tag{1}$$

The corresponding manipulator Jacobian $J(q) \in \mathbb{R}^{3\times3}$ relates joint velocities to EE velocity:

$$\dot{p} = J(q)\,\dot{q} \tag{2}$$

The torque sensor at each joint reports a signed integer count T_i, which is converted to interaction torque in N·m via a calibration scale of 0.01N·m/count. For the wrist, $\tau_{h,3} = -0.01 \cdot T_3/\alpha_3$, where $\alpha_3 = -0.5128$ for the wrist gear pair. The resulting vector $\boldsymbol{\tau}_h = [\tau_{h,1}, \tau_{h,2}, \tau_{h,3}]^{\mathrm{T}}$represents the user's volitional driving torque applied through the cuff–handle interface.

2.3 Gravity compensation

The exoskeleton's gravitational load is compensated joint-wise through a closed-form model derived from the dynamic parameters:

$$\tau_{g,j}(q_j) = A_j cos(q_j + \varphi_j) + b_j,\ j \in \{1,2\} \tag{3}$$

Here A_j is the gravitational amplitude, φ_j a phase offset that absorbs the joint-frame reference, and b_j a constant accounting for torque-sensor bias and cuff pre-load. The gravity-compensation parameters in Eq. (3) were identified from measured static joint torques. The calibrated compensator rendered the device quasi-transparent. Here, quasi-transparency means that the residual uncompensated torque is small enough to keep the limb from drifting passively. Joints 1 and 2 are gravitationally decoupled in the device's kinematic arrangement, and joint 3 actuates only a lightweight distal link whose gravitational moment is negligible.

As shown in Fig.3, with no external force applied and the limb removed from the cuff, the device was driven to a grid of configurations spanning the working range and sampled at 6×6 poses. The steady-state torque readings were averaged over 5 s per pose.

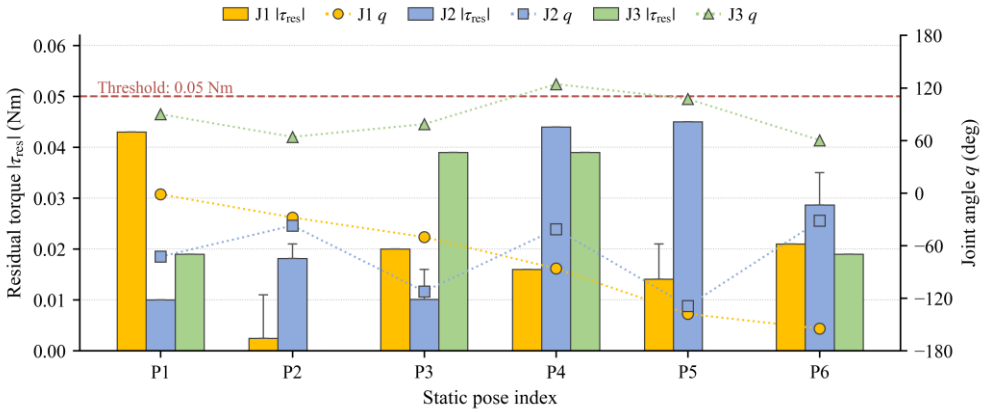


Fig. 3. Identification and validation of the gravity-compensation model.

2.4 Movement path generation in Cartesian space

To translate a clinically meaningful joint-space exercise prescription into an admissible Cartesian movement region, we precompute a discrete reference path $\{\boldsymbol{x}_k\}_{k=0}^{N-1}$. Given a smooth clinician-defined joint-space exercise path parameterized by a progression variable, the corresponding EE waypoints are obtained through forward kinematics.

$$\boldsymbol{q}(s) = \boldsymbol{q}_{\text{off}} + s \,\Delta\, \boldsymbol{q} \tag{4}$$

with $\Delta\boldsymbol{q} = [-\frac{\pi}{2}, -\frac{\pi}{4}, \frac{\pi}{2}]^{\mathrm{T}}$representing a clinician-defined elbow flexion, forearm pronation and wrist flexion exercise envelope, the corresponding EE waypoints are $\boldsymbol{x}_k = \mathrm{FK}\left(\boldsymbol{q}(s_k)\right)$, $s_k = \frac{k}{N-1}$. This piecewise-linear path serves both as the geometric centerline of the tunnel and as the source of the goal pose $\boldsymbol{p}_g = \boldsymbol{x}_{N-1}$ and goal-tangent direction $\hat{\boldsymbol{t}}_g$ used for terminal detection.

2.5 Multi-joint synergistic isokinetic resistance formulation

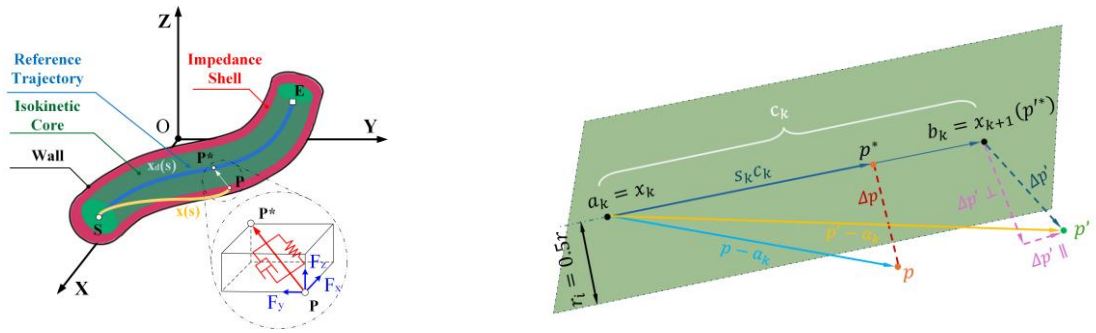
The isokinetic resistance is defined independently of the spatial tunnel. Human-applied joint torque is first mapped through the admittance law to an unconstrained joint-velocity command.

$$\begin{cases} \mathbf{v}_a = \mathbf{J}(\mathbf{q})\,\dot{\mathbf{q}}_{\text{adm}}, \\ \alpha_v = \min\left(1, \dfrac{v_{\text{iso}}}{\|\mathbf{v}_a\|}\right), \\ \dot{\mathbf{q}}_{\text{cmd}} = \alpha_v\,\dot{\mathbf{q}}_{\text{adm}} \end{cases} \tag{5}$$

where $\dot{\mathbf{q}}_{\text{adm}}$ denotes the joint-velocity command generated by the admittance-based velocity generator, $\mathbf{J}(\mathbf{q})$ is the manipulator Jacobian, and $\mathbf{v}_a$ is the corresponding unconstrained EE linear velocity vector. v_{iso} denotes the prescribed maximum Cartesian linear speed of the EE, and α_v is the velocity-scaling factor. The speed-limited command $\dot{\mathbf{q}}_{\text{cmd}}$ therefore satisfies the commanded EE speed constraint $\|\mathbf{J}(\mathbf{q})\,\dot{\mathbf{q}}_{\text{cmd}}\| \le v_{\text{iso}}$.

2.6 Variable-impedance tunnel constraint formulation

2.6.1 Tunnel geometry and distance measure



(a) (b)

Fig. 4. Concept of the variable-impedance tunnel constraint: (a) Tubular safe corridor defined about the Cartesian reference path, comprising the isokinetic core of radius r_i, the surrounding impedance shell, and the outer wall at radius r; (b) Projection of two end-effector positions onto segment k. Primed symbols denote the endpoint case, in which the projection onto the segment is clipped at $\mathbf{b}_k(s_k{}' = 1)$. The tangential component $\Delta\mathbf{p}'_{\parallel}$ is defined along the endpoint tangent $\mathbf{t}_{\text{end}}$.

The concept of the variable-impedance tunnel is shown in Fig.4(a). At each control cycle, the current EE position $\mathbf{p} \in \mathbb{R}^3$ is projected onto the prescribed polyline centerline $\mathcal{C} = \{\mathbf{x}_k\}_{k=1}^{N}$. In Fig.4(b), for the *k th* line segment, defined by $\mathbf{a}_k = \mathbf{x}_k, \mathbf{b}_k = \mathbf{x}_{k+1}, \mathbf{c}_k = \mathbf{b}_k - \mathbf{a}_k$, the scalar projection coefficient is computed as

$$s_k = \mathrm{clip}\left(\frac{(\mathbf{p} - \mathbf{a}_k)^{\mathrm{T}}\mathbf{c}_k}{\|\mathbf{c}_k\|^2}, 0, 1\right) \tag{6}$$

where $\mathrm{clip}(\cdot, 0, 1)$ bounds the argument within [0, 1]. The closest point candidate on this segment is therefore

$$\mathbf{p}_k^c = \mathbf{a}_k + s_k\mathbf{c}_k \tag{7}$$

The nearest segment index is selected by

$$k^* = \arg\min_{k\in\mathcal{J}} \|\mathbf{p} - \mathbf{p}_k^c\|, \mathbf{p}^* = \mathbf{p}_{k^*}^c \tag{8}$$

where $\mathcal{J}$ denotes the search set. For real-time implementation, $\mathcal{J}$ is chosen as a 24-segment local window centered at the previous nearest-segment index, while a full global rescan is performed every 50 control cycles to suppress accumulated index drift.

The local unit tangent of the centerline at $\mathbf{p}^*$ is defined as

$$\hat{\mathbf{t}} = \begin{cases} \dfrac{\mathbf{c}_{k^*}}{\|\mathbf{c}_{k^*}\|}, & s_{k^*} \in (0,1), \\ \hat{\mathbf{t}}_{\text{end}}, & s_{k^*} \in \{0,1\}. \end{cases} \tag{9}$$

where $\hat{\mathbf{t}}_{\text{end}}$ is assigned as the unit direction of the adjacent segment at the corresponding endpoint. The EE deviation from the centerline is then decomposed into tangential and normal components as $\Delta\mathbf{p} = \mathbf{p} - \mathbf{p}^*$, $\Delta\mathbf{p}_\parallel = (\Delta\mathbf{p}^{\mathrm{T}}\hat{\mathbf{t}})\hat{\mathbf{t}}$, $\Delta\mathbf{p}_\perp = \Delta\mathbf{p} - \Delta\mathbf{p}_\parallel$. Accordingly, the radial deviation from the tunnel centerline is given by $d_{min} = \|\Delta\mathbf{p}_\perp\|$. Two coaxial cylindrical boundaries are constructed around the polyline centerline to define the admissible motion tunnel. The inner radius is set to $r_i = 0.5r$, and the outer radius is $r = 0.10$ m.

2.6.2 Region selection with hysteresis

To prevent control chattering near the boundaries, the region label $\mathcal{R} \in \{0,1,2\}$ (isokinetic / impedance / wall) is selected via a hysteresis rule with a 3 mm dead-band h:

$$\mathcal{R}_{k+1} = \begin{cases} 2, & d_{min} \geq r + h \\ 0, & d_{min} \leq r_i - h \\ \mathcal{R}_k, & \text{transition near } r_i \text{ or } r \\ 1, & \text{otherwise.} \end{cases} \tag{10}$$

2.6.3 Region 0: Isokinetic core

Inside the inner core, the patient's volitional intent is preserved. The commanded EE behavior is purely admittance-like, mapping the human-applied torque to a target joint velocity:

$$\tau_{c,i} = \tau_{h,i} + \tau_{g,i}(\boldsymbol{q}) \tag{11}$$

where $\tau_{g,i}$ is the gravity-compensation torque, b_i is a small joint-level damping coefficient that suppresses encoder-noise-induced oscillation, and $k_{\tau 2\dot{q}}^{(i)}$ is the per-joint torque-to-velocity admittance gain. To suppress ripple, a per-joint dead zone is applied:

$$\tilde{\tau}_{c,i} = \operatorname{sgn}(\tau_{c,i}) \cdot \max\left(|\, \tau_{c,i} \,| - \tau_i^{\mathrm{dz}}, 0\right) \tag{12}$$

with $\boldsymbol{\tau}^{\mathrm{dz}} = [0.05, 0.05, 0.05]^{\mathrm{T}}$N·m, followed by a low-pass exponential filter

$$\dot{q}_{i,\mathrm{cmd}} = \alpha_i \dot{q}_{i,\mathrm{tgt}} + (1 - \alpha_i)\, \dot{q}_{i,\mathrm{prev}} \tag{13}$$

with smoothing factors $\boldsymbol{\alpha} = [0.75, 0.88, 0.75]^{\mathrm{T}}$ tuned to match each joint's inertial response. To further mitigate spikes, particularly for the elbow flexion motor, a per-step torque-rate limiter caps $|\, \Delta\tilde{\tau}_{c,i} \,|$ at $[0.8, 1.2, 0.35]^{\mathrm{T}}$ N·m/cycle.

2.6.4 Region 1: Impedance shell

Within the impedance shell, a linear spring–damper field acts in the radial direction to gently restore the EE toward the centerline. The Cartesian virtual force is

$$\boldsymbol{F}_{\mathrm{vir}} = -K_p\, \Delta\boldsymbol{p}_\perp - K_d\, \dot{\boldsymbol{p}}_\perp \tag{14}$$

with $K_p = 100$ N/m, $K_d = 4.5$ N·s/m, and $\dot{\boldsymbol{p}}_\perp$ the radial component of the EE velocity computed from $\boldsymbol{J}\dot{\boldsymbol{q}}$. The corresponding joint torque is obtained via the manipulator Jacobian transpose,

$$\boldsymbol{\tau}_{\text{vir}} = \boldsymbol{J}^{\mathsf{T}}(\boldsymbol{q})\, \boldsymbol{F}_{\text{vir}} \tag{15}$$

The fused command is

$$\boldsymbol{\tau}_{\text{cmd}} = \boldsymbol{\tau}_h + \boldsymbol{\tau}_{\text{vir}} + \boldsymbol{\tau}_g(\boldsymbol{q}) - \text{diag}(\boldsymbol{b})\, \dot{\boldsymbol{q}} \tag{16}$$

where $\boldsymbol{\tau}_h$ is the torque sensor measured. The desired joint velocity is then generated through the same admittance map and low-pass filter as in region 0.

A boundary tangential damping term is additionally engaged when $d > d_{\text{dmp}} = 0.05$ m, smoothly ramped via

$$\boldsymbol{F}_{\text{vir}} = -K_t \left(\frac{d - d_{\text{dmp}}}{r - d_{\text{dmp}}}\right) \dot{\boldsymbol{p}}_{\parallel} \tag{17}$$

with $K_t = 6$N·s/m. Eq. (17) increases tangential damping as the user approaches the outer wall to mitigate wall-grazing oscillations, which is a phenomenon analogous to shear damping in haptic virtual-fixture literature.

2.6.5 Region 2: Wall

When $d > r$, the EE is geometrically outside the tunnel. A normal-direction barrier force is applied,

$$\boldsymbol{F}_{\text{vir}} = -(K_p^{\text{w}}(d - r) + K_d^{\text{w}}\, v_n^{+})\hat{\boldsymbol{n}} \tag{18}$$

where $\hat{\boldsymbol{n}} = \Delta\boldsymbol{p}_{\perp}/d$is the outward radial unit normal, $v_n^{+} = \max(\dot{\boldsymbol{p}} \cdot \hat{\boldsymbol{n}}, 0)$ damps only outward motion (the wall is one-sided), and $(K_p^{\text{w}}, K_d^{\text{w}}) = (6, 2)$. Importantly, in this region the controller does not apply tangential auto-guidance: progress along the path remains under volitional control.

2.6.6 Geometric boundary-protection layer

In addition to the soft impedance forces, two protective layers limit outward motion near the tunnel boundary:

(i) Outward-velocity barrier. For each cycle inside the tunnel, the maximum admissible outward EE velocity is

$$v_n^{\max} = \frac{r - \delta - d}{\Delta t} \tag{19}$$

with safety margin $\delta = 10^{-4}$m and $\Delta t = 0.02$s. If the predicted outward speed $v_n$exceeds $v_n^{\max}$, the joint command is uniformly scaled by $v_n^{\max}/v_n$.

(ii) Hard projection. Only when $d > r - 0.01$m (i.e., near the outer wall), a one-step look-ahead is performed: the predicted joint state $\boldsymbol{q}^{+} = \boldsymbol{q} + \dot{\boldsymbol{q}}_{\text{cmd}}\Delta t$ is fed through the FK to obtain $\boldsymbol{p}^{+}$. If $\| \Delta\boldsymbol{p}_{\perp}^{+} \| > r - \delta$, a 10-iteration bisection search shrinks the step:

$$\dot{\text{q}}_{\text{cmd}} \leftarrow \lambda^{\star}\, \dot{\text{q}}_{\text{cmd}}, \quad \lambda^{\star} = \max\{\lambda \in [0,1] \mid \| \text{FK}(\text{q} + \lambda\dot{\text{q}}_{\text{cmd}}\Delta\text{t}) - \text{p}^{*} \|_{\perp} \leq \text{r} - \delta\} \tag{20}$$

Should the EE already lie outside the tunnel at the cycle's start, an inverse-kinematics step projects it back onto the wall via $\text{IK}_{\text{near}}(\boldsymbol{q}, \boldsymbol{p}^{*} + (r - \delta)\hat{\boldsymbol{n}})$.

This two-tier scheme uses a lightweight velocity check and reserves the more computationally demanding projection for motion near the boundary. Both steps act on commanded motion.

3 Materials and experiments

3.1 Experimental platform and apparatus

All experiments were conducted on the 3-DOF upper-limb exoskeleton described in Section 2.1. Joint states were obtained from the on-board encoders, and human–robot interaction torques τ_h were measured by the joint-

mounted torque sensors (Section 2.2). The VITC controller was executed on the STM32 microcontroller at a fixed control period Δt=0.02 s. EE position and velocity were reconstructed offline from the logged joint states through the forward-kinematics and Jacobian models.

For the sEMG study (Section 3.4), muscle activity was recorded with an sEMG device at 1 kHz. The isotonic condition used a set of hand-held dumbbells weighing 3 kg, 5 kg, and 7.5 kg.

3.2 Isokinetic control performance

3.2.1 Experiment objective

This experiment evaluated how closely the reconstructed EE speed $||\boldsymbol{v_{ee}}||$ approached each nominal setting during active driving. Peak speed overshoot was also quantified.

3.2.2 Experiment protocol

Inside the isokinetic core, the admittance law maps the human-applied torque to a joint-velocity command, and the Cartesian speed limiter caps the commanded EE speed at $\boldsymbol{v_{nom}}$. Direction and initiation remain with the operator. The magnitude of the EE velocity approaches the nominal value when the speed limiter is engaged. The movement tasks were based on proprioceptive neuromuscular facilitation (PNF). The operator performed two multi-joint diagonal patterns: the upper-limb flexion/extension diagonals and a spiral pattern. The selected movement patterns are also relevant to functional actions such as self-feeding. Each pattern was executed in active mode. These patterns co-excite all three joints along clinically meaningful trajectories, rather than along a single axis.

Each pattern was performed at three nominal EE speeds: low $\boldsymbol{v_{nom}}$=0.05 m/s, medium 0.10 m/s, and high 0.15 m/s. For each speed, the operator was instructed to drive the device as continuously and forcefully as was comfortable so as to keep the limiter saturated. The commanded velocity, the reconstructed EE velocity $\|v_{\mathbf{ee}}\| = \|J\dot{q}\|$, and the joint angle were logged.

3.3 Variable-impedance tunnel constraint validation

3.3.1 Experiment objective

To demonstrate, from the measured EE trajectory and the controller's region telemetry, that the variable-impedance tunnel (i) leaves volitional motion unconstrained inside the isokinetic core, (ii) progressively restores the EE toward the centerline within the impedance shell and (iii) limits outward motion near the outer wall.

3.3.2 Experiment protocol

Two conditions were run on the same reference path as described in Section 3.2.2. In the baseline condition, the operator performed one complete back-and-forth traversal while keeping the EE within the isokinetic core ($d \leq r_i$=0.05 m); the impedance and wall fields were thereby never engaged (R=0), establishing the unconstrained, transparent behavior of the device along the prescribed corridor.

In the perturbed condition, the operator deliberately drove the EE radially outward across the inner boundary and toward the outer wall. The radial spring–damper field acted in the impedance shell, and the one-sided barrier and predictive projection acted near the outer boundary.

During each trial, joint torque, EE trajectory, EE velocity, and joint angles were recorded synchronously. The trajectory evolution was first used to examine whether the EE remained inside the prescribed tunnel. Joint torque responses were analyzed together with the radial deviation to evaluate the restoring action generated by the tunnel constraint.

3.4 sEMG-based muscle activation assessment in multi-joint synergistic isokinetic training

3.4.1 Experiment objective

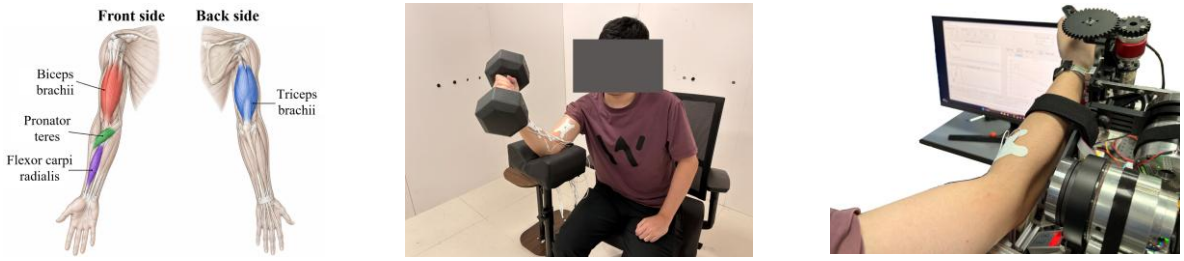
The experiment compared acute sEMG amplitudes and temporal patterns in four muscles during multi-joint synergistic isokinetic exercise with the exoskeleton and isotonic free-weight exercise. The external load and movement constraints differed between conditions.

3.4.2 Participants

Five healthy male adults were recruited (age:26.6±3.3, height:170.8±4.1 cm, body mass:69.0±6.5 kg). The study received ethics approval (Approval No. HIT-2024077), and all participants provided written informed consent before participation.

3.4.3 Experiment protocol

Participants were instructed to perform a PNF-based diagonal movement in both conditions. The task involved elbow flexion and extension, forearm pronation and supination, and wrist flexion, resembling the multi-joint motion used to reach toward the mouth.



(a) (b) (c)

Fig. 5. The experiment protocol: (a) Muscle site selection; (b) Isotonic training; (c) Isokinetic training.

As shown in Fig. 5(a), four target muscles of the dominant arm were recorded, one per channel, as summarized in Table 1. A reference electrode was placed at the wrist.

Table 1 Target muscles, recording channels, and primary actions.

Channel	Muscle	Primary action	Electrode site (SENIAM)
CH1	Biceps brachii (BB)	Elbow flexion / forearm supination	Belly of the long head, midway between the innervation zone and the distal tendon
CH2	Triceps brachii (TB)	Elbow extension	Belly of the long head, on the line acromion–olecranon
CH3	Pronator teres (PT)	Forearm pronation	Proximal–medial forearm, over the muscle belly along the fiber direction
CH4	Flexor carpi radialis (FCR)	Wrist flexion / radial deviation	Anterior forearm, over the muscle belly along the fiber direction

Raw sEMG signals were band-pass filtered 20–450 Hz, 4th-order zero-phase Butterworth, notch-filtered at 50 Hz, full-wave rectified, and converted to a linear envelope 4 Hz low-pass and RMS.

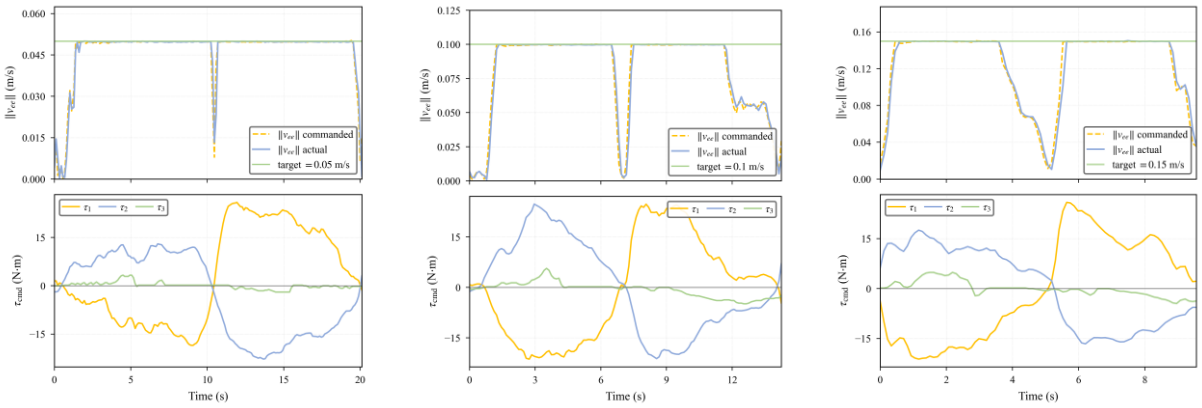
In the isotonic condition (Fig. 5(b)), participants performed the movement without the exoskeleton while holding the heaviest dumbbell they could lift from the available masses of 3, 5, and 7.5 kg. In the isokinetic condition (Fig. 5(c)), participants performed the prescribed movement with the exoskeleton in VITC mode at a nominal EE speed of 0.05 m/s. The protocol specified three sets per condition, with 2 min of rest between sets. Condition order was randomized across participants.

For each muscle and metric, trial-level values were averaged within each participant and condition. The analysis included three trials per condition for four participants and two isotonic trials and three isokinetic trials for the remaining participant. Each participant contributed one paired observation per muscle and metric (n = 5). Between-condition differences were evaluated using two-sided paired t-tests. With only five paired differences per comparison, the distribution of the differences could not be assessed reliably, so the t-test results were interpreted as exploratory. The effect estimate for each comparison was the mean paired difference (isokinetic minus isotonic), reported in μV with an unadjusted 95% t-based confidence interval.

4 Results

4.1 Isokinetic speed tracking performance

Fig. 6 shows the commanded and reconstructed EE speeds at nominal settings of 0.05, 0.10, and 0.15 m/s. During sustained driving, the reconstructed speed approached the nominal settings. The reported peak EE speeds were 0.0500, 0.1001, and 0.1505 m/s, respectively, with small overshoots at the two higher settings.



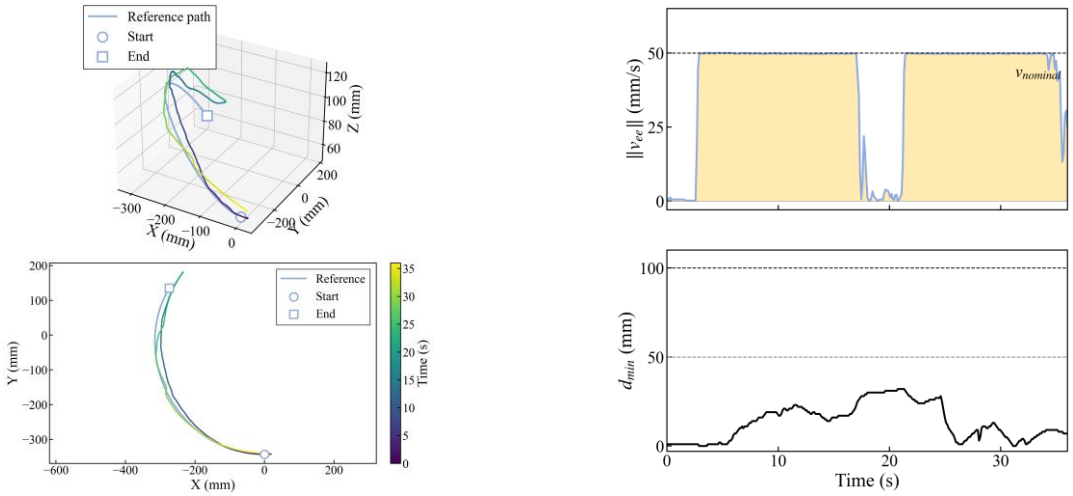
(a) (b) (c)

Fig. 6. EE speed-tracking performance under isokinetic regulation at three nominal speeds: (a) $\boldsymbol{v}_{\mathbf{nom}}$=0.05 m/s; (b) $\boldsymbol{v}_{\mathbf{nom}}$=0.1 m/s; (c) $\boldsymbol{v}_{\mathbf{nom}}$=0.15 m/s.

4.2 Trajectory deviation correction under variable-impedance tunnel constraint

4.2.1 Baseline condition

Fig. 7 shows the controller behavior during a representative 36 s baseline trial. As illustrated in Fig. 7(a)–(b), the operator completed one reciprocating cycle with one repetition. The EE speed $||\boldsymbol{v}_{\mathbf{ee}}||$ was strictly maintained at or below the nominal velocity $\boldsymbol{v}_{\mathbf{nom}}$, with zero frames exceeding the limit. The path deviation d_{min} remained below the isokinetic-zone boundary (50 mm) throughout the entire trial, with a peak of 32 mm and a median of 12 mm. It indicates that the EE adhered tightly to the predefined path.

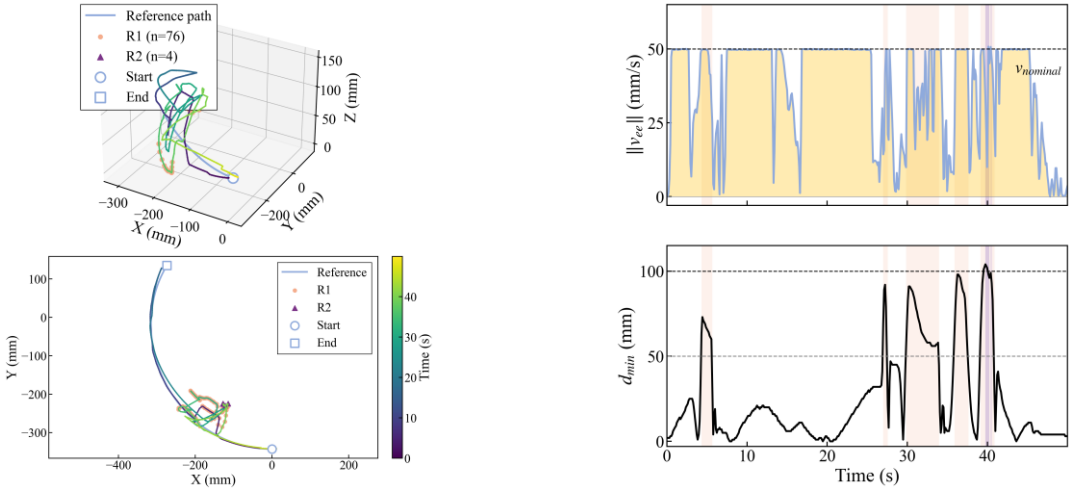


(a) (b)

Fig. 7. Controller behavior during the baseline trial of one reciprocating cycle without external perturbation: (a) EE motion trajectory in Cartesian space; (b) EE speed and path deviation.

4.2.2 Perturbation condition

Under the perturbation condition (Fig. 8), the operator deliberately drove the EE outward during five intervals of one back-and-forth traversal. The constraint mechanism engaged automatically as d_{min} exceeded the R0 boundary, with 17.5% of frames operating in the impedance region R1 and 0.9% momentarily entering the block region R2. The controller invoked predictive projection 19 times.



(a) (b)

Fig. 8. Controller behavior under transverse perturbations applied during one reciprocating cycle: (a) EE motion trajectory in Cartesian space and the R_i occurrence during the process; (b) EE speed $\| v_{ee} \|$and minimum path-deviation distance d_{min}.

The maximum radial deviation reached 104 mm, 4 mm beyond the nominal outer boundary of 100 mm (Fig. 8(b)). The EE subsequently returned inside the tunnel. The radial deviation returned to 50 mm or less within 2 s in four of the five events. The other event involved a sustained outward push lasting approximately 4 s.

4.2.3 Comparison

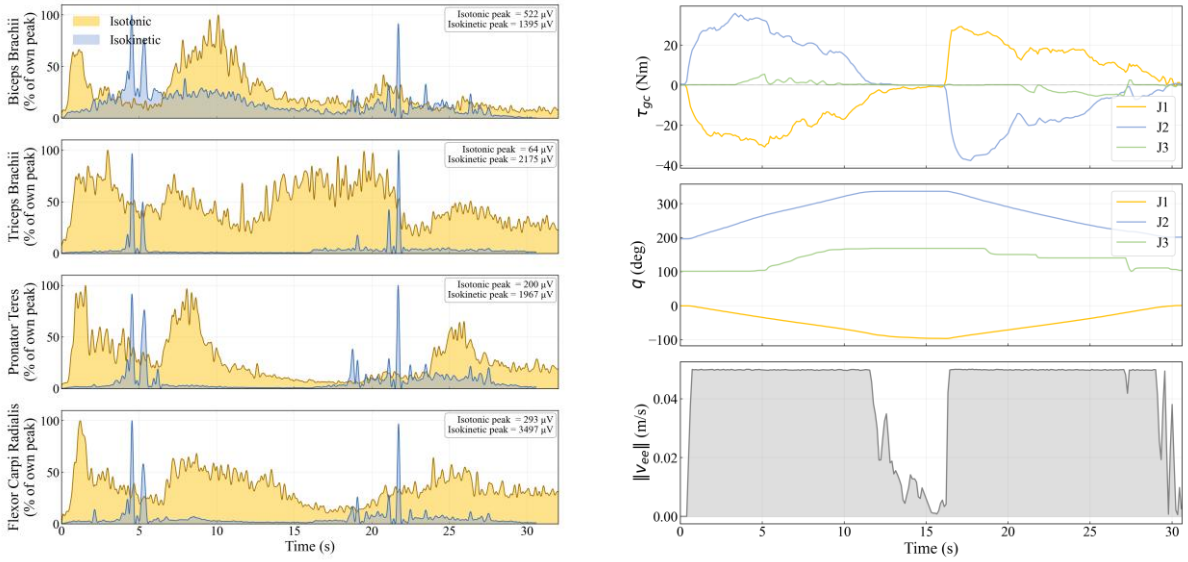
The baseline trial stayed within the free-motion core, while the perturbation trial engaged the impedance shell and outer-wall response. The controller acted to return the EE toward the reference path after the observed deviations. The transient crossing of the outer boundary quantifies the extent of the overshoot in this trial.

4.3 Muscle activation during multi-joint synergistic isokinetic and isotonic training

4.3.1 Representative single-trial results

Fig. 9 shows an example from Subject 1. Fig. 9(a) compares the four sEMG envelopes for the two exercise conditions. Each envelope is expressed as a percentage of its own peak to illustrate temporal patterns, and the panel annotations give the corresponding peak amplitudes in μV. In this example, the exoskeleton condition showed several brief bursts in the recorded muscles.

Fig. 9(b) shows the joint angles, gravity-compensated joint torques, and reconstructed EE speed during the first exoskeleton trial. J1, J2, and J3 denote elbow flexion/extension, forearm pronation/supination, and wrist flexion/extension, respectively.



(a) (b)

Fig. 9. Representative trial data for Subject 1: (a) sEMG envelopes of the four target muscles, normalized to their respective peaks for display; (b) Joint torques, joint angles, and EE speed during a representative exoskeleton trial.

4.3.2 Group-level sEMG comparisons

Table 2 and Fig. 10 summarize the group-level sEMG results for the four muscles. Mean sEMG amplitudes were higher in the isokinetic condition for all 12 muscle–metric combinations. Biceps brachii RMS was higher in the isokinetic condition in all five participants. The mean paired difference was 268.3 μV (unadjusted 95% CI, 155.0 to 381.6 μV). A similar pattern was observed for the triceps brachii, with the largest between-condition difference appearing in the peak amplitude. However, all *p* values from the exact Wilcoxon signed-rank tests were 0.0625 or greater.

Table 2 Surface electromyography amplitude metrics during isotonic and isokinetic exercise. Condition values are mean ± SD across five participant-level averages (*$p < 0.05$, **$p < 0.01$).

Muscle	Metric	Isotonic (μV)	Isokinetic (μV)	Paired difference (95% CI), μV	p (t-test)
BB	RMS	261.1 ± 79.5	529.4 ± 57.7	268.3 (155.0~381.6)	0.0028**
	MAV	167.8 ± 59.0	240.1 ± 40.5	72.3 (21.7~122.9)	0.0166*
	Peak	2167 ± 660	6922 ± 2577	4754.6 (617.6~8891.6)	0.0332*
TB	RMS	89.4 ± 23.7	361.7 ± 169.5	272.3 (38.7~506.0)	0.0318*
	MAV	52.6 ± 10.2	114.2 ± 37.8	61.6 (7.1~116.0)	0.0349*
	Peak	902 ± 336	8198 ± 4107	7296.2 (1578.4~13014.0)	0.0240*
PT	RMS	109.2 ± 34.1	198.6 ± 111.7	89.4 (−94.7~273.5)	0.2488
	MAV	69.8 ± 21.9	84.3 ± 35.1	14.5 (−49.2~78.2)	0.5617
	Peak	1005 ± 312	3500 ± 2443	2495.4 (−1200.5~6191.4)	0.1341
FCR	RMS	146.3 ± 53.9	346.5 ± 165.6	200.1 (−45.8~446.1)	0.0868
	MAV	106.0 ± 41.0	153.5 ± 42.1	47.5 (−13.2~108.2)	0.0954
	Peak	1078 ± 366	6645 ± 4689	5567.3 (−1206.8~12341.4)	0.0846

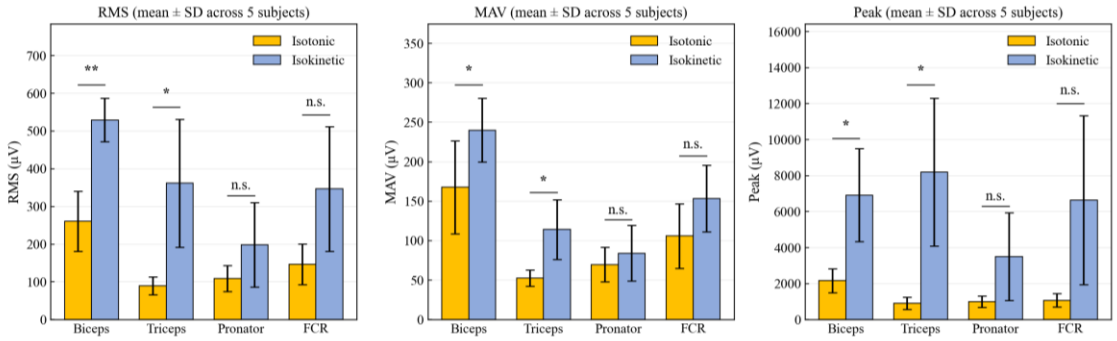


Fig. 10 Group-level sEMG amplitude metrics across the five subjects, comparing the isotonic and isokinetic conditions for the four target muscles (*$p < 0.05$, **$p < 0.01$).

5 Discussion

5.1 Multi-joint synergistic isokinetic control performance

The controller regulated Cartesian EE speed during a multi-joint movement and permitted voluntary variation in the free-motion core. In the speed-tracking trials, reconstructed speeds approached the three nominal settings, with small peak overshoots at 0.10 and 0.15 m/s. This task-space approach applies a ceiling to linear EE speed, whereas a conventional single-joint dynamometer regulates angular velocity about its axis [25,26]. Individual joint speeds can vary even when the EE reaches the prescribed ceiling.

5.2 Interpretation of the control and safety behaviors

The tunnel trials separate what each region contributes. In the baseline trial, the EE remained within the tunnel core, where the restoring force was inactive. During the perturbation trial, the controller activated the radial spring–damper field as the EE moved outside the core. Near the outer boundary, it applied the outward-velocity barrier and predictive projection. The radial deviation peaked at 104 mm, beyond the nominal outer radius of 100 mm, before the EE returned inside the tunnel.

5.3 Neuromuscular implications of multi-joint synergistic isokinetic training

The sEMG results characterize the acute neuromuscular response to multi-joint synergistic isokinetic training. Biceps brachii RMS was higher during exoskeleton exercise in all five participants. This finding remains exploratory given the small sample and the limited resolution of the exact Wilcoxon sensitivity analysis. The gravitational moment arm changes during free-weight exercise, while the exoskeleton applies resistance through its task-space velocity constraint. The movement followed the proprioceptive neuromuscular facilitation diagonals [27], and the sEMG signals were acquired and processed following established recommendations for electrode placement and signal conditioning [28,29]. Brief bursts in the representative exoskeleton trial may reflect deceleration or stabilization demands. Differences in loading and kinematics could also affect sEMG amplitudes. Joint motors and torque sensing enable estimation of interaction torque, range of motion, and velocity at each exoskeleton joint. The tunnel permits limited spatial variation around the prescribed path.

5.4 Limitations and future work

The sEMG study involved only five healthy male participants in a single session, and therefore demonstrates feasibility and acute neuromuscular responses rather than clinical efficacy. EE kinematics were reconstructed from joint states, and the gravity-compensation model did not explicitly account for limb weight. The present controller limits EE speed. Joint-level isokinetic control, inter-joint coordination, and muscle shortening or lengthening velocities were not evaluated. Future work will therefore extend the framework to higher-DOF shoulder–elbow–wrist exoskeletons and integrate joint-level kinematic and physiological information for individualized coordination assessment and training.

6 Conclusions

This work extends conventional single-joint isokinetic exercise to multi-joint synergistic isokinetic resistance training and introduces VITC to preserve the intended movement pattern. The reconstructed EE speed approached the prescribed settings, and the maximum tunnel-boundary overshoot was 4 mm in the perturbation trial. With five healthy male participants, the sEMG results showed significantly higher activation of the biceps brachii and triceps brachii, while the pronator teres and flexor carpi radialis also exhibited increased activation. Future work will focus on patient validation, individualized parameter adaptation, and extension to higher-DOF upper-limb exoskeletons.

Acknowledgements This work was funded by the National Natural Science Foundation of China under Grant 62403170, Support by Self-Planned Task (NO. SKLRS202505C) of State Key Laboratory of Robotics and Systems (HIT)， Shenzhen Science and Technology Program under Grant JCYJ20240813105129039, and QNXMC20250701091903005. The authors used (GPT-6.1, sol) as a language-editing tool to improve grammar, clarity, and readability. The AI tool was not used for data analysis, data generation, image processing, or scientific content creation. All outputs were carefully reviewed and verified by the authors, who take full responsibility for the final content.

Conflict of interest Author Honghai Liu is an Editorial Board Member for ENGINEERING Health and Rehabilitation Engineering. The paper was handled by another Editor and has undergone a rigorous peer review process. Author Honghai Liu was not involved in the journal's peer review or decisions related to this manuscript. All other authors declare that they have no conflict of interest or financial conflicts to disclose.

Data availability statement The datasets used during the study should be uploaded to a public database or available upon reasonable request, especially for research articles.

Compliance with ethics guidelines The human-participant study received ethics approval (Approval No. HIT-2024077). All participants provided written informed consent before participation. The study was conducted in accordance with the Declaration of Helsinki and applicable institutional and national ethical guidelines.

References

1. Rose C G, Deshpande A D, Carducci J, Brown J D. The road forward for upper-extremity rehabilitation robotics. *Current Opinion in Biomedical Engineering*, 2021, **19**: 100291.

2. Liu Z, Zhang J, Zhou H, Cao R, Sheng Y, Song Z, Zhang B, Zhang M, Liu H. A Dual-Fatigue Speed Guidance Model for Isokinetic Training: Cognitive and sEMG-Based Physiological Fatigue Approach. *IEEE Transactions on Neural Systems and Rehabilitation Engineering*, 2025, **33**: 2311-2321.
3. De Iaco L, Veerbeek J M, Ket J C F, Kwakkel G. Upper limb robots for recovery of motor arm function in patients with stroke: a systematic review and meta-analysis. *Neurology*, 2024, **103**(8): e209495.
4. Fareh R, Elsabe A, Baziyad M, Kawser T, Brahmi B, Rahman M H. Will your next therapist be a robot?—a review of the advancements in robotic upper extremity rehabilitation. *Sensors*, 2023, **23**(11): 5054.
5. Dalla Gasperina S, Roveda L, Pedrocchi A, Braghin F, Gandolla M. Review on patient-cooperative control strategies for upper-limb rehabilitation exoskeletons. *Frontiers in Robotics and AI*, 2021, **8**: 745018.
6. Guo W, Gao J, Dawazhuoma, Mi X, Ciwang, Bianba. A meta-analysis of randomized controlled trials: evaluating the efficacy of isokinetic muscle strengthening training in improving knee osteoarthritis outcomes. *Journal of Orthopaedic Surgery and Research*, 2025, **20**(1): 95.
7. van der Woude D R, Ruyten T, Bartels B. Reliability of muscle strength and muscle power assessments using isokinetic dynamometry in neuromuscular diseases: a systematic review. *Physical Therapy*, 2022, **102**(8): pzac099.
8. van Melick N, van der Weegen W, van der Horst N. Quadriceps and hamstrings strength reference values for athletes with and without anterior cruciate ligament reconstruction who play popular pivoting sports, including soccer, basketball, and handball: a scoping review. *Journal of Orthopaedic & Sports Physical Therapy*, 2022, **52**(3): 142–155.
9. Hu B, et al. Disturbance rejection speed control based on linear extended state observer for isokinetic muscle strength training system. *IEEE Transactions on Automation Science and Engineering*, 2023, **20**(3): 1962–1971.
10. Feng Y, Wu H, Ren J, et al. Power-free knee rehabilitation robot for home-based isokinetic training. *Nature Communications*, 2025, **16**: 2347.
11. Zhou Z, Wan Y, Su Y, Li Y, Hu B, Yu H. Research on design and control methods of a lightweight upper limb joint isokinetic rehabilitation training equipment. *Frontiers in Bioengineering and Biotechnology*, 2024, **12**: 1430372.
12. Qian W, Liao J, Lu L, et al. CURER: a lightweight cable-driven compliant upper limb rehabilitation exoskeleton robot. *IEEE/ASME Transactions on Mechatronics*, 2023, **28**(3): 1730–1741.
13. Yang Z, Guo S, Liu Y, Kawanishi M, Hirata H. A task performance-based sEMG-driven variable stiffness control strategy for upper limb bilateral rehabilitation system. *IEEE/ASME Transactions on Mechatronics*, 2023, **28**(2): 792–803.
14. Noronha B, et al. Soft lightweight wearable robots to support the upper limb in activities of daily living: a feasibility study on chronic stroke patients. *IEEE Transactions on Neural Systems and Rehabilitation Engineering*, 2022, **30**: 1401–1411.
15. Sharifi M, Azimi V, Mushahwar V K, Tavakoli M. Impedance learning-based adaptive control for human–robot interaction. *IEEE Transactions on Control Systems Technology*, 2022, **30**(3): 1345–1358.
16. Li Y, Ren J, Shu T, Yuan F, Feng Y. Spinal neuromotor rehabilitation using a portable isokinetic training robot. *Nature*, 2026, **654**: 932–940.
17. Zarrin R S, Zeiaee A, Langari R. A variable-admittance assist-as-needed controller for upper-limb rehabilitation exoskeletons. *IEEE Robotics and Automation Letters*, 2024, **9**(6): 5903–5910.
18. Pezeshki L, Sadeghian H, Keshmiri M, Chen X, Haddadin S. Cooperative assist-as-needed control for robotic rehabilitation: a two-player game approach. *IEEE Robotics and Automation Letters*, 2023, **8**(5): 2852–2859.
19. Li N, Yang Y, Li G, et al. Multi-sensor fusion-based mirror adaptive assist-as-needed control strategy of a soft exoskeleton for upper limb rehabilitation. *IEEE Transactions on Automation Science and Engineering*, 2024, **21**(1): 475–487.
20. Onfiani D, Caramaschi M, Biagiotti L, Pini F. Optimizing design and control methods for using collaborative robots in upper limb rehabilitation. *IEEE/ASME Transactions on Mechatronics*, 2025, 30(6): 4849–4861.

21. Sun J, Foroutani Y, Rosen J. Virtually constrained admittance control using feedback linearization for physical human-robot interaction with rehabilitation exoskeletons. *IEEE/ASME Transactions on Mechatronics*, 2025, 30(2): 898–909.
22. Asl H J, Yamashita M, Narikiyo T, Kawanishi M. Field-based assist-as-needed control schemes for rehabilitation robots. *IEEE/ASME Transactions on Mechatronics*, 2020, 25(4): 2100–2111.
23. Liu Q, Liu Y, Li Y, Zhu C, Meng W, Ai Q, Xie S Q. Path planning and impedance control of a soft modular exoskeleton for coordinated upper limb rehabilitation. *Frontiers in Neurorobotics*, 2021, 15: 745531.
24. Liu Z, Zhou H, Sheng Y, Song Z, Liu H. A Human-Centered Prototype of a 3-DOF Upper Rehabilitation Exoskeleton with Multi-Objective Optimization. *2025 IEEE International Conference on Real-time Computing and Robotics (RCAR)*, Toyama, Japan: IEEE, 2025, pp. 395–400.
25. Dvir Z. Isokinetics: Muscle Testing, Interpretation and Clinical Applications. 2nd ed. Edinburgh: *Churchill Livingstone*, 2004.
26. Kannus P. Isokinetic evaluation of muscular performance: implications for muscle testing and rehabilitation. *International Journal of Sports Medicine*, 1994, **15**(S1): S11–S18.
27. Adler S S, Beckers D, Buck M. PNF in Practice: An Illustrated Guide. 4th ed. Berlin: *Springer*, 2014.
28. Hermens H J, Freriks B, Disselhorst-Klug C, Rau G. Development of recommendations for SEMG sensors and sensor placement procedures. *Journal of Electromyography and Kinesiology*, 2000, **10**(5): 361–374.
29. De Luca C J. The use of surface electromyography in biomechanics. *Journal of Applied Biomechanics*, 1997, **13**(2): 135–163.